Received: 9 August 2022 | Revised: 19 January 2023 | Accepted: 15 February 2023 | Published on: 31 March 2023

DOI: 10.1002/mrm.29627

Magnetic Resonance in Medicine

TECHNICAL NOTE

To mask or not to mask? Investigating the impact of accounting for spatial frequency distributions and susceptibility sources on QSM quality

Anders Dyhr Sandgaard[1] | **Noam Shemesh**[2] | **Sune Nørhøj Jespersen**[1,3] | **Valerij G. Kiselev**[4]

[1]Center for Functionally Integrative Neuroscience, Department of Clinical Medicine, Aarhus University, Aarhus, Denmark

[2]Champalimaud Research, Champalimaud Centre for the Unknown, Lisbon, Portugal

[3]Department of Physics and Astronomy, Aarhus University, Aarhus, Denmark

[4]Division of Medical Physics, Department of Radiology, Faculty of Medicine, University of Freiburg, University Medical Center Freiburg, Freiburg, Germany

Correspondence
Valerij G. Kiselev, Division of Medical Physics, Department of Radiology, Faculty of Medicine, University of Freiburg, University Medical Center Freiburg, Killian Str. 5a, 79106, Freiburg, Germany.
Email: valerij.kiselev@uniklinik-freiburg.de

Funding information
Danmarks Frie Forskningsfond, Grant/Award Number: Grant/Award Number: 8020-00158B

Purpose: Estimating magnetic susceptibility using MRI depends on inverting a forward relationship between the susceptibility and measured Larmor frequency. However, an often-overlooked constraint in susceptibility fitting is that the Larmor frequency is only measured inside the sample, and after successful background field removal, susceptibility sources should only reside inside the same sample. Here, we test the impact of accounting for these constraints in susceptibility fitting.

Theory and Methods: Two different digital brain phantoms with scalar susceptibility were examined. We used the MEDI phantom, a simple phantom with no background fields, to examine the effect of the imposed constraints for various levels of SNR. Next, we considered the QSM reconstruction challenge 2.0 phantom with and without background fields. We estimated the parameter accuracy of openly-available QSM algorithms by comparing fitting results to the ground truth. Next, we implemented the mentioned constraints and compared to the standard approach.

Results: Including the spatial distribution of frequencies and susceptibility sources decreased the RMS-error compared to standard QSM on both brain phantoms when background fields were absent. When background field removal was unsuccessful, as is presumably the case in most in vivo conditions, it is better to allow sources outside the brain.

Conclusion: Informing QSM algorithms about the location of susceptibility sources and where Larmor frequency was measured improves susceptibility fitting for realistic SNR levels and efficient background field removal. However, the latter remains the bottleneck of the algorithm. Allowing for external sources regularizes unsuccessful background field removal and is currently the best strategy in vivo.

KEYWORDS

fitting, inverse problem, Larmor frequency, magnetic susceptibility, quantitative susceptibility mapping

This is an open access article under the terms of the Creative Commons Attribution-NonCommercial-NoDerivs License, which permits use and distribution in any medium, provided the original work is properly cited, the use is non-commercial and no modifications or adaptations are made.
© 2023 The Authors. *Magnetic Resonance in Medicine* published by Wiley Periodicals LLC on behalf of International Society for Magnetic Resonance in Medicine.

1 | INTRODUCTION

Magnetic susceptibility $\chi(r)$ can vary greatly across different tissue types,[1] making it a highly desirable contrast mechanism reflecting the local chemical composition in biological tissues. A method for mapping $\chi(r)$ with MRI is dubbed QSM,[2–8] which aims to determine a voxel-specific scalar magnetic susceptibility with promising results.[9–11] In QSM, the examined tissue is effectively assumed to be isotropic with slowly varying magnetic susceptibility. This assumption allows the Larmor frequency shift, $\Omega(r)$, to be written as a convolution of the susceptibility $\chi(r)$ with a Lorentz-corrected dipole kernel.[12] Extensions to this simplified model incorporating heterogenous tissue microstructure have also been proposed.[13–15]

The inverse problem of estimating $\chi(r)$ from the measured $\Omega(r)$ has proven to be very difficult. In particular, the inversion is singular as the dipole kernel contains a zero-valued cone. Besides the ill-posed nature of the inversion, and irrespective of the assumed model for tissue complexity, an additional challenge arises from the limited volume in which the Larmor frequency is measured,[16] which we refer to as the sample. Moreover, due to the non-local effects of susceptibility, the sample in fact does not include all sources of the induced magnetic field within it: for example, magnetization induced in the body affects the Larmor frequency measured in the brain. The effect of such sources is reduced by so-called background field removal techniques,[17] but present QSM algorithms[7,8,18–22] utilizing the Fourier domain to solve the inverse problem result in magnetic susceptibility distributed within the whole FOV, that is, not limited to the actual sample volume.

Here, we investigate the effect of informing susceptibility fitting algorithms that the Larmor frequency is only measured inside the sample, and constraining susceptibility sources to the volume in which the Larmor frequency has been measured and corrected by the background field removal. Using digital susceptibility brain phantoms, we evaluate the parameter accuracy of openly available QSM algorithms for varying peak signal SNR and background fields, with and without the proposed constraint.

2 | THEORY

2.1 | Forward problem - finding Ω

We consider the relationship between the induced Larmor frequency shift $\Omega(r)$ in a sample and measured at discrete sampling positions. For simplicity, we assume each discrete location is characterized by a scalar susceptibility $\chi(r)$ as a result of averaging over the microstructure. Hence, the sample resembles an isotropic media with voxel-wise constant $\chi(r)$, as in conventional QSM. The relationship between $\chi(r)$ and $\Omega(r)$ can then be written as a linear matrix–vector equation

$$\vec{\Omega} = \mathbf{A}\vec{\chi}, \text{(Forward model)}. \tag{1}$$

Here, $\vec{\Omega}$ and $\vec{\chi}$ are $N \times 1$ vectors denoting the measured Larmor frequencies and susceptibility sources in vector form, respectively, where N is the number of voxels in the FOV. The matrix $\mathbf{A}$ is an $N \times N$ symmetric matrix describing the induced frequency shift in the FOV due to the voxel magnetization in the main field. The diagonal of $\mathbf{A}$ is zero for isotropic liquids, but if the sample exhibits anisotropic magnetic tissue properties, it acquires a non-zero diagonal[14]; we do not consider such media here. $\mathbf{A}\vec{\chi}$ amounts to a linear convolution[2–4,23] of $\mathbf{A}$ with $\vec{\chi}$, which can conveniently be implemented in Fourier space using the convolution theorem. Notice that Eq. (1) predicts a non-zero frequency in the whole FOV.

2.2 | Inverse problem - finding χ

The aim of QSM is to estimate $\vec{\chi}$ from the measured $\vec{\Omega}$ using the known $\mathbf{A}$ in Eq. (1). This amounts to inverting (deconvolving with) $\mathbf{A}$, which is a well-known ill-posed problem due to the functional form of the dipole field. The list of algorithms with various weights and regularizations to invert Eq. (1) is long; see References 8, 19–22, 24–26 for a few examples. Prior to fitting (assuming an ideal signal acquisition), $\vec{\Omega}$ must be extracted from the signal phase. Subsequently, the phase must be unwrapped.[17,27] Finally, contributions from external magnetized sources must be accurately removed for Eq. (1) to represent sources residing inside the sample, a task for which numerous different algorithms exist.[17]

If contributions from external sources are successfully eliminated, we are left with the following two points (**P1** and **P2**) of consideration:

(**P1**) Eq. (1) predicts a non-zero frequency $\vec{\Omega}$ in the whole FOV, while we only measure it inside the sample due to lack of useful signal outside.

The lack of signal may stem from an absent of water or low SNR. If the sample is embedded in a medium such as agarose, the frequency will likewise be affected by chemical shifts, which is not included in Eq. (1). We account for the lack of frequency measurements outside the sample by introducing a sample mask $\mathbf{M}$ (not to be confused with magnetization), an $N \times N$ diagonal matrix with $M_{ii} = 1$ if

15222594, 2023, 1, Downloaded from https://onlinelibrary.wiley.com/doi/10.1002/mrm.29627 by Cochrane Portugal, Wiley Online Library on [19/05/2023]. See the Terms and Conditions (https://onlinelibrary.wiley.com/terms-and-conditions) on Wiley Online Library for rules of use; OA articles are governed by the applicable Creative Commons License

and only if voxel i is inside the sample. Then the information about the actually measured volume is captured by replacing $\mathbf{A} \rightarrow \mathbf{MA}$. This substitution is effectively done when minimizing the SNR-weighted least squares.

(**P2**) Susceptibility $\vec{\chi}$ should only be non-zero inside the sample upon successful background-field-removal.

We enforce **P2** using the same mask $\mathbf{M}$, so $\vec{\chi} \rightarrow \mathbf{M}\vec{\chi}$.

Constraints similar to **P1** and **P2** have previously been used to remove background fields,[28] but here we emphasize that such measures must also be taken for internal sources to represent the measured data correctly. Including **P1** and **P2** into Eq. (1) forms the new inverse problem we wish to solve, and which is the focus of the present study:

$$\min_{\vec{\chi}} \|\vec{\Omega} - \mathbf{MAM}\vec{\chi}\|_2^2, \text{(Inverse problem)}. \qquad (2)$$

Here $\|\cdot\|_\vartheta$ denotes the l_ϑ-norm ($\vartheta = 2$ in Eq. 2). Similar to conventional weighted least squares in QSM,[8] $\mathbf{M}$ limits the utility of solving the inverse problem exclusively in Fourier space as it becomes a convolution also in Fourier space. This suggests the use of iterative least squares to estimate $\vec{\chi}$.

3 | METHODS

3.1 | Digital brain phantom simulation

All simulations were performed in Matlab (The MathWorks, Natick, MA, USA). We tested the minimization problem, Eq. (2), on two different brain phantoms of increasing complexity.

3.1.1 | MEDI phantom

The first phantom is a digital brain phantom with a spatially varying scalar susceptibility $\vec{\chi}_{\text{GT}}$ provided with the MEDI toolbox[18,24,25,29,30] and their MRI signal generator. This produced a complex multi-echo gradient signal $\mathrm{S}(t) = \frac{|\chi_{\text{GT}}|}{\max(|\chi_{\text{GT}}|)} \exp(-i\Omega t) + (\varepsilon(t) + i\eta(t))$ with independent Gaussian noise $N\left(0, \frac{1}{\text{SNR}^2}\right)$ in the real and imaginary signal channels for each voxel. We investigated a peak signal SNR ranging from 10 to 200, and with no noise (SNR = ∞). Using the MEDI toolbox, the Larmor frequency Ω used for fitting χ was estimated based on fitting a complex exponential to the signal. Background-field removal and phase-unwrapping was not necessary as no external fields was present in the phantom, and the phase was kept below $\pm 2\pi$.

3.1.2 | QSM reconstruction challenge 2.0 phantom

The second digital phantom considered was the reconstruction challenge 2.0 (RC2) phantom[31,32] with a downscaled isotropic resolution of 1 mm and signal SNR of 100. The RC2 phantom includes two versions of MRI complex signals: (a) with no external sources (similar to the MEDI phantom) and (b) including realistic background fields from biological sources outside the brain such as air cavities, bone, fat, etc. In both cases the signal magnitude does not directly correspond to susceptibility (in contrast to the MEDI phantom). We extracted the Larmor frequency by fitting a complex exponential to the signal with code supplied with the MEDI toolbox. Then we used SEGUE[27] for phase unwrapping and LBV[33] for background field removal (only in case (b), with depth and peel set to 8).

3.1.3 | Effect on true in vivo and ex vivo data fitting

All animal experiments were preapproved by the competent institutional and national authorities and carried out according to European Directive 2010/63.

Since true ex vivo or in vivo images do not have a known ground truth, we chose to focus this study on digital brain phantoms. However, we also investigated the effect of including masks on real MRI data using the QSM reconstruction challenge[34] 1.0 (RC1) in vivo data with 12 sample orientations and acquired ex vivo mouse brain data at ultra-high field (16.4 T). For RC1, we implemented masks into COSMOS[8] using the LSMR[35] algorithm.

3.2 | Fitting algorithms

To be on par with current standards, we took openly available iterative QSM algorithms and measured their performance in estimating the ground truth scalar susceptibility $\vec{\chi}_{\text{GT}}$ for each digital phantom. Next, we implemented the masks into the algorithms according to Eq. (2) and compared the results to calculations without masking. We investigated MEDI[18,24,25,29,30] and two additional $l1$ and $l2$ regularized iterative algorithms,[20] which we denote F$l1$ and F$l2$, respectively. Including the masks described by **P1** and **P2**, we obtain the following minimization algorithms:

$$\textbf{MEDI}: \min_{\vec{\chi}} \left\{ \|\mathbf{W}_1 \nabla \mathbf{M}\vec{\chi}\|_1 + \lambda \left\| \mathbf{W}_2(\vec{\Omega} - \mathbf{AM}\vec{\chi}) \right\|_2^2 \right\}, \text{(Liu et al. 2012)},$$

15222594, 2023, 1, Downloaded from https://onlinelibrary.wiley.com/doi/10.1002/mrm.29627 by Cochrane Portugal, Wiley Online Library on [19/05/2023]. See the Terms and Conditions (https://onlinelibrary.wiley.com/terms-and-conditions) on Wiley Online Library for rules of use; OA articles are governed by the applicable Creative Commons License

$$\mathbf{Fl1}: \min_{\vec{\chi}} \left\{ \alpha \left\| \nabla \mathbf{M} \vec{\chi} \right\|_1 + \frac{1}{2} \left\| (\vec{\Omega} - \mathbf{MAM}\vec{\chi}) \right\|_2^2 \right\}, \text{(Bilgic et al. 2012)},$$

$$\mathbf{Fl2}: \min_{\vec{\chi}} \left\{ \beta \left\| \nabla \mathbf{M} \vec{\chi} \right\|_2^2 + \frac{1}{2} \left\| (\vec{\Omega} - \mathbf{MAM}\vec{\chi}) \right\|_2^2 \right\}, \text{(Bilgic et al. 2012)}.$$

$\mathbf{W}_1$ is a structural weighting matrix derived from the gradient of the signal magnitude, while $\mathbf{W}_2$ is proportional to signal magnitude to compensate for noise variations (see References 18,20). Hence, $\mathbf{W}_2$ already accounts for **P1** in MEDI, while the $\mathbf{M}\vec{\chi}$ terms are the modifications added in this study to fulfill **P2**. Notice that **P2** is imposed explicitly in the regularization term, as $\mathbf{W}_1$ does not null the susceptibility gradient outside the brain.

3.3 | Analysis and optimal parameter values

Fitting tolerances, maximum iterations and so forth. were kept as the default settings for all algorithms (we refer to the source code).

We computed the normalized RMS-error (RMSE) relative to ground truth across the whole brain for all brain phantoms. Before computing the RMSE, the susceptibility fits, and ground truth were demeaned. For the RC2 phantom, the RMSE was also computed in reference to their mean susceptibility from CSF in ventricles. Additionally, RMSE was computed only in (1) white matter (WM), gray matter (GM), and thalamus; and (2) deep GM nuclei (DGN). The fitting parameters λ, α, β in Eqs. (3)–(5) were optimized by the RMSE of the whole brain (optimization shown in Figures S1 and S2 in supplementary information).

4 | RESULTS

4.1 | MEDI phantom

Figure 1 shows the RMSE between the fitted $\vec{\chi}$ and ground truth $\vec{\chi}_{\mathrm{GT}}$ for the MEDI phantom, for all considered methods, and for different SNRs. Across all three algorithms (MEDI, F*l1*, F*l2*), adding masks to the fitting algorithms reduced the error. The largest improvement was clearly in F*l1* and F*l2*, while MEDI improved a few percent. Figure 2 shows the susceptibility fits and difference from ground truth for three different SNRs. Here the improvement is clear for F*l1* and F*l2* for all SNRs, while changes in MEDI were most noticeable in the noiseless case.

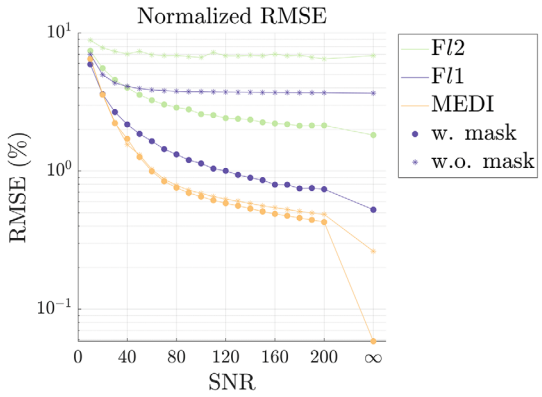

FIGURE 1 RMSE of MEDI phantom: The normalized and demeaned RMSE decreases for increasing SNR. The decrease is larger for fitting with masking.

4.2 | RC2 phantom

Figure 3 shows the RMSE between the $\vec{\chi}$ and $\vec{\chi}_{\mathrm{GT}}$ for the RC2 phantom for the cases with or without external sources (w. BF in bottom row/w.o. BF in upper row, respectively), while Figures 4, 5 shows the corresponding susceptibility fits and difference to ground truth. We observed an improvement for all considered methods when including the masks to the algorithm (red rim is RMSE when fitting with masks), but only in the absence of background fields. When external sources were present, the frequency map after background field removal and unwrapping deviated 44% RMSE compared to the ground truth, even though we eroded the brain eight layers during BFR. This error carried over to the susceptibility fitting. Hence, allowing external sources provided a form of regularization for the imperfect estimation of background fields.

4.3 | Effect on in vivo and ex vivo data fitting

For in vivo images, we found a 24% root-mean-squared difference between demeaned fits with and without masks. Here we report the difference between the two fits due to lack of ground truth. A similar difference was found in ex vivo data. A full description along with susceptibility fits can be found in the supplementary information (Figures S3 and S4). Here, the large changes in vivo may be indicative of the unsuccessful background field removal which results in great differences, while this appears to be less of a problem ex vivo.

15222594, 2023, 1, Downloaded from https://onlinelibrary.wiley.com/doi/10.1002/mrm.29627 by Cochrane Portugal, Wiley Online Library on [19/05/2023]. See the Terms and Conditions (https://onlinelibrary.wiley.com/terms-and-conditions) on Wiley Online Library for rules of use; OA articles are governed by the applicable Creative Commons License

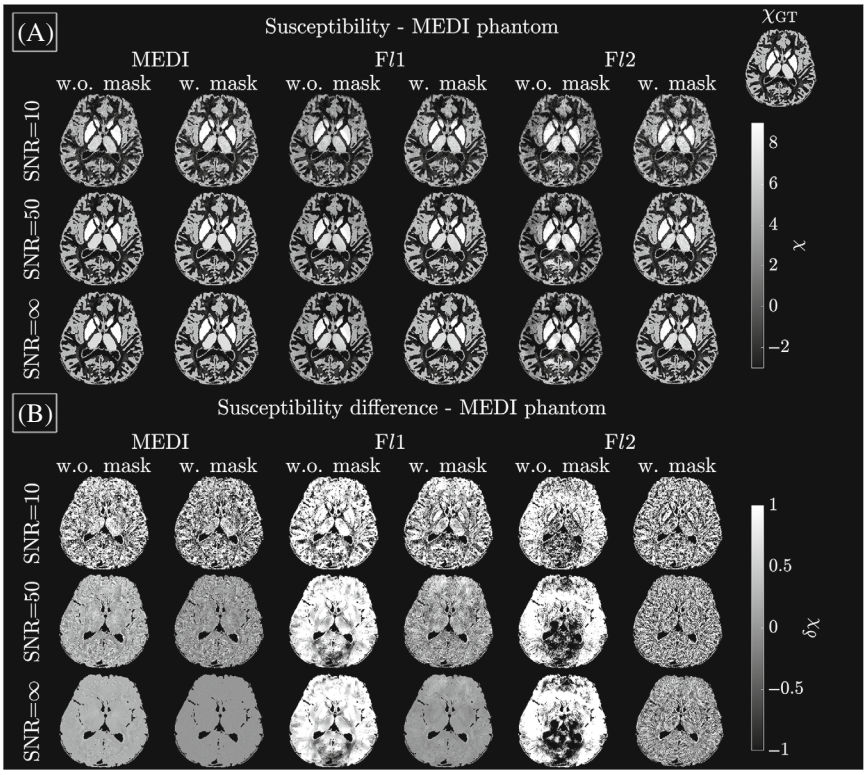

FIGURE 2 Representative susceptibility maps and their relative errors from a mid-axial slice in MEDI phantom: (**A**) The resulting susceptibility maps from fitting MEDI phantom with or without masks, using MEDI, F*l1* or F*l2*, respectively. Rows correspond to different SNRs from 10 to ∞. (**B**) The difference to the ground truth. The color bar is truncated at ±1 with units in ppm.

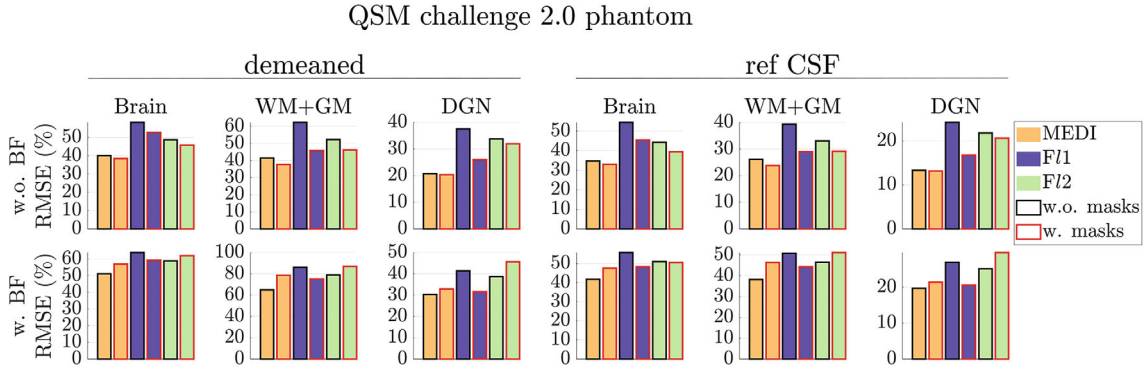

FIGURE 3 RMSE of RC2 phantom: The normalized RMSE is shown across the whole brain (left), WM and GM (middle), and deep gray matter (right). RMSE is presented either demeaned or referenced to CSF in ventricles. Upper row is RMSE for RC2 phantom without background fields (w.o. BF) and lower is with (w. BF).

5 | DISCUSSION

5.1 | Simulations

5.1.1 | MEDI phantom

Using optimized regularization parameters in the simulations, we found improvements in fitting quality by incorporating masks in the fitting algorithms. For the MEDI phantom, the improvement increased for increasing SNR. For MEDI, the RMSE decreased by 5% when SNR was 100, and in the limit of no noise, the RMSE dropped by 78%. For F*l2* the decrease was 63% and 75%, respectively, and for F*l1* the decrease was 70% and 93%, respectively. This demonstrates that even the MEDI algorithm, which is tailored for fitting this exact type of phantom based on its regularization, has visible differences from ground truth solely due to not informing about source localization. The large improvement on F*l1* and F*l2* stems from adding both **P1** and **P2**, while for MEDI we only added **P2**.

5.1.2 | QSM 2.0 reconstruction (RC2) phantom

In general, we found that referencing to CSF produced the lowest RMSE. This makes sense, as the largest sources of error between the susceptibility fit and the ground truth

15222594, 2023, 1, Downloaded from https://onlinelibrary.wiley.com/doi/10.1002/mrm.29627 by Cochrane Portugal, Wiley Online Library on [19/05/2023]. See the Terms and Conditions (https://onlinelibrary.wiley.com/terms-and-conditions) on Wiley Online Library for rules of use; OA articles are governed by the applicable Creative Commons License

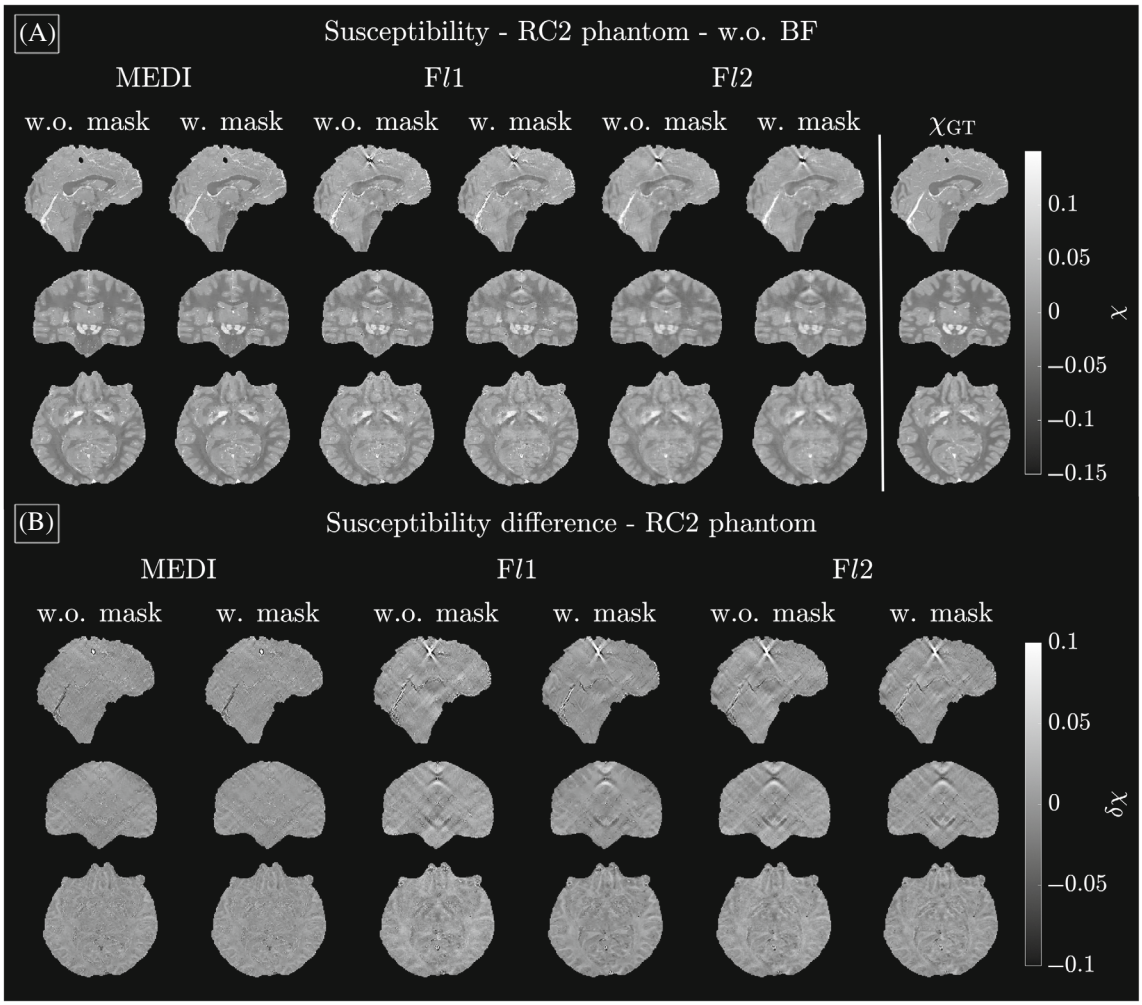

FIGURE 4 Representative susceptibility maps and their relative errors from multiple slice directions in RC2 phantom without background fields (w.o. BF). (**A**) The resulting susceptibility maps from fitting RC2 phantom with or without masks, using MEDI, F*l1* or F*l2*, respectively. (**B**) The difference to the ground truth. The color bar is truncated at ±0.1. Streaking is visible for F*l1* and F*l2*, but suppressed in MEDI. Otherwise, all maps are visually very similar to ground truth.

are from veins. When demeaning, the distributions will then not align optimally, in comparison to referencing to CSF where the susceptibility estimate should be close to the ground truth. For that reason, we discuss here the changes in RMSE wrt. referencing to CSF.

For the RC2 phantom without external sources, we increased the parameter accuracy in susceptibility values even after unwrapping. The highest accuracy was achieved using MEDI Eq. (5), with decreases in RMSE around 5% in the whole brain, 10% in GM and WM tissue, and 2% in DGN. This improvement agrees with the MEDI phantom results since we used an SNR of 100. For a noiseless simulation, we expect this improvement to be higher. F*l1* decreased in RMSE around 16% in the whole brain, 26% in GM and WM tissue, and 31% in DGN. F*l2* decreased in RMSE around 11% in the whole brain, 12% in GM and WM tissue, and 1% in DGN.

For the RC2 phantom with external sources, where background field removal was needed prior to QSM, we generally see that allowing sources outside produces the lowest RMSE. The highest parameter accuracy was again achieved using MEDI Eq. (5). Here, fitting with the mask increased the RMSE around 13% in the whole brain, 13% in GM and WM tissue, and 8% in DG. For F*l1*, fitting with masks decreased the RMSE around 10% in the whole brain, 26% in GM and WM tissue, and 24% in DGN. For F*l2*, fitting with masks decreased the RMSE below 1% in the whole brain, and increased 6% in GM and WM tissue, and 18% in DGN. In all cases, more regularization was needed when fitting with the constraint on allowed susceptibility sources (cf. Figure S2 in supplementary information). Hence, even though we found lower RMSE for F*l1*, it was at the expense of increased smoothing of susceptibility maps, which may not be favorable.

15222594, 2023, 1, Downloaded from https://onlinelibrary.wiley.com/doi/10.1002/mrm.29627 by Cochrane Portugal, Wiley Online Library on [19/05/2023]. See the Terms and Conditions (https://onlinelibrary.wiley.com/terms-and-conditions) on Wiley Online Library for rules of use; OA articles are governed by the applicable Creative Commons License

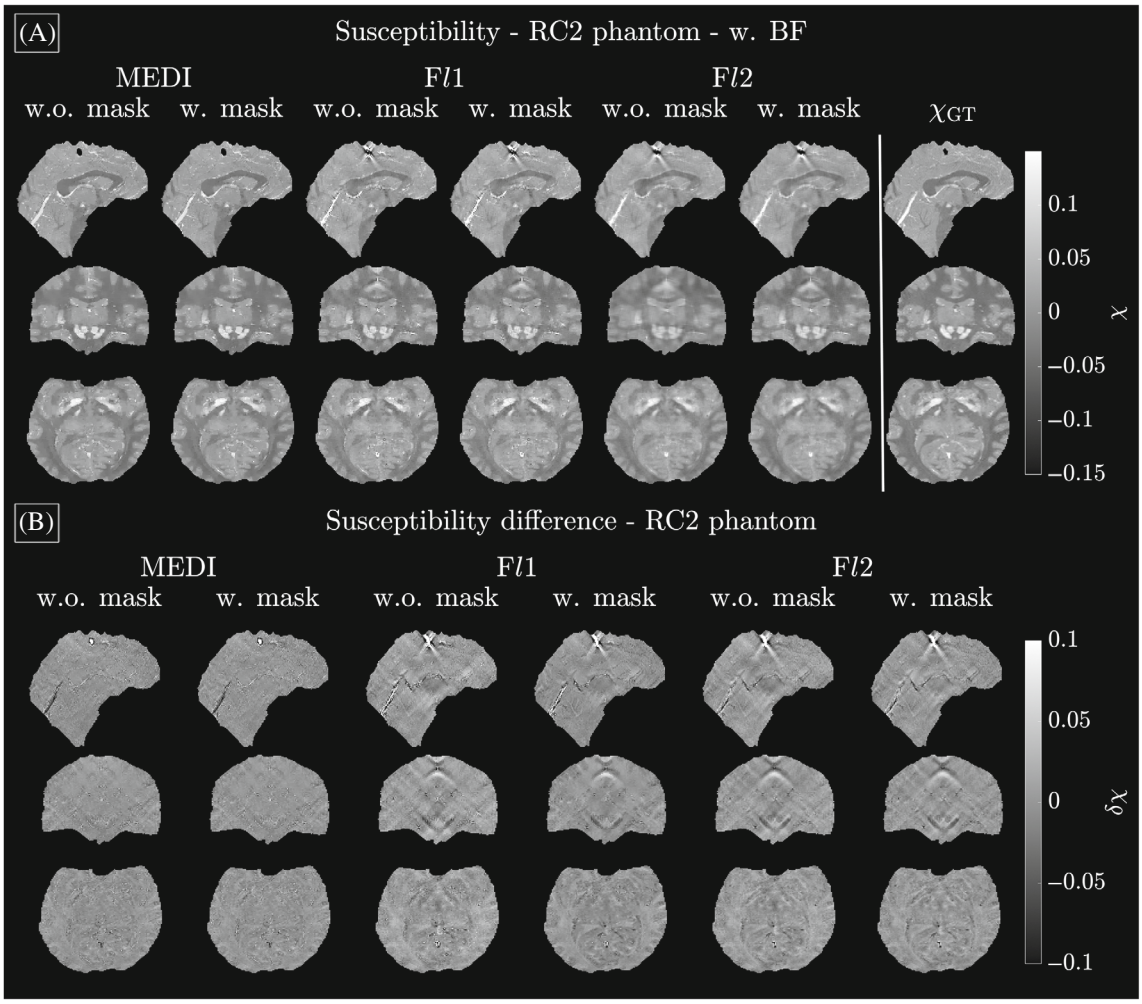

FIGURE 5 Representative susceptibility maps and their relative errors from multiple slice directions in RC2 phantom with background fields (w. BF). (**A**) The resulting susceptibility maps from fitting RC2 phantom with or without masks, using MEDI, F*l1* or F*l2*, respectively. (**B**) The difference to the ground truth. The color bar is truncated at ±0.1. A large erosion of the brain is clearly visible compared to Figure 4. This is due to background field removal, where eight layers were peeled off. Again, streakings are visible for F*l1* and F*l2*, but MEDI also shows misestimation of the calcification (black circle in upper row), which can be seen in the difference map. Besides streaking in F*l1* and F*l2*, all maps look visually similar to ground truth.

5.2 | To mask or not to mask?

The absence of signal outside the sample is an unavoidable feature in MRI, and not including this limitation can lead to erroneous susceptibility estimations. The imposed error can be understood by considering the inverse problem, Eq. (2), using the iterative conjugate gradient method.[36] Here, the solution $\vec{\chi}_{k+1}$ at iteration $k+1$, depends on all the previous residual vectors $\vec{r}_k = \vec{\Omega} - \mathbf{A}\vec{\chi}_k$. Since $\mathbf{A}\vec{\chi}_k$ generates a frequency in the whole FOV, no matter the constraint imposed on $\vec{\chi}$, and $\vec{\Omega}$ is zero outside the sample, every residual $\vec{r}_k$ obtains an error, as the fitting algorithm will try to find a solution that reproduces the zeroes in $\vec{\Omega}$, which in turn leads to erroneous solutions $\vec{\chi}_{k+1}$. This error can in principle be avoided by introducing a sample mask $\mathbf{M}$, so the residual vectors spanning the solutions become $\vec{r}_k = \vec{\Omega} - \mathbf{MA}\vec{\chi}_k$. This constraint can also be included, as in MEDI, through an SNR weight $\mathbf{W}_2$ on the fidelity term.

The second constraint on allowed positions of susceptibility sources arose not directly because of unavoidable limitations in how we measure, but rather due to how $\vec{\Omega}$ is processed before fitting. Namely, as external sources to the sample produce large slowly varying frequency contributions inside the sample, such contributions must be removed prior to susceptibility fitting. While many different algorithms exist for this purpose,[17] common to them all is that an ROI (e.g., $\mathbf{M}$) must be defined, where frequency contributions from sources outside the ROI is removed. This leaves us with the natural assumption that the only remaining frequency contributions originate from sources within that ROI. If the ROI is $\mathbf{M}$, the residual vectors in our

15222594, 2023, 1, Downloaded from https://onlinelibrary.wiley.com/doi/10.1002/mrm.29627 by Cochrane Portugal, Wiley Online Library on [19/05/2023]. See the Terms and Conditions (https://onlinelibrary.wiley.com/terms-and-conditions) on Wiley Online Library for rules of use; OA articles are governed by the applicable Creative Commons License

conjugate gradient example should be $\vec{r}_k = \vec{\Omega} - \mathbf{MAM}\vec{\chi}_k$, to avoid sources outside **M** when estimating $\vec{\chi}_{k+1}$.

However, when background field removal is incomplete, the susceptibility fits $\vec{\chi}_{k+1}$ will incur an error, and additional errors arise due to the constraint itself. This is due to the estimated Larmor frequency including field errors induced by sources outside the sample, and these errors are optimally "regularized" by allowing for sources outside the sample to compensate.

5.3 | Recommendations for QSM fitting

To mask or not to mask thus depends on the type of study. Digital phantoms are highly popular for practicing solving the inverse problem, and reconstruction challenges[32] have already been carried out. For such studies, no outside sources are to be found, and one can therefore achieve a boost in parameter accuracy by constraining positions of susceptibility. We therefore recommend using the proposed constraints for such studies.

For in vivo QSM, background field removal is paramount, but results in non-negligible errors in the frequency map (for the RC2 phantom, the frequency map had a 44% RMSE compared to the ground truth frequency map without external sources, even after heavy erosion). This indicates the background field removal is the central problem of the current QSM algorithms (disregarding anisotropic tissues). Incomplete removal of the background field implies the presence of residual sources outside the brain. Hence, one will achieve the best susceptibility maps by allowing sources outside. Nevertheless, in all cases, we found that it improved parameter accuracy to inform the algorithm about where the frequency was measured, which is evident from the MEDI algorithm.

5.4 | Limitations

We illustrated the level of improvement achievable in representative existing algorithms, and how easy these corrections can be incorporated. The matrix **A** may also contain additional complexity, for example in terms of mesoscopic effects, which introduces diagonal terms to **A** capturing local structural and/or magnetic anisotropy.[13,14]

Simulating the effect of masking on digital phantoms, enabled a comparison to a known ground truth and control over the amount of noise in the MRI signal and the background field. However, while testing major confounds, other artifacts may also hamper the performance boost, for example, eddy current distortions, sample motion etc. Such effects could be included in the phantom and studied as well.

6 | CONCLUSION

We demonstrated an improvement in susceptibility fitting results for digital brain phantoms by incorporating the constraints that the Larmor frequency is only measured inside the sample. When the phantoms did not include brain-external sources, susceptibility fitting was further improved by constraining susceptibility sources to not reside outside the sample.

ACKNOWLEDGMENTS

We thank Shemesh lab members, especially PhD Cristina Chavarrías and MSc Beatriz Cardoso for assisting with MRI experiments, Prof. Mark D. Does and Dr. Kevin Harkins from Vanderbilt University for the REMMI pulse sequence, and Prof. Jürgen R. Reichenbach from University Hospital Jena for insightful discussions. This study is funded by the Independent Research Fund (grant 8020-00158B). Open Access funding enabled and organized by Projekt DEAL.

ORCID

Noam Shemesh https://orcid.org/0000-0001-6681-5876
Sune Nørhøj Jespersen https://orcid.org/0000-0003-3146-4329
Valerij G. Kiselev http://orcid.org/0000-0002-5349-5399

REFERENCES

1. Fukunaga M, Li TQ, Van Gelderen P, et al. Layer-specific variation of iron content in cerebral cortex as a source of MRI contrast. *Proc Natl Acad Sci U S A*. 2010;107:3834-3839. doi:10.1073/pnas.0911177107
2. Salomir R, de Senneville BD, Moonen CT. A fast calculation method for magnetic field inhomogeneity due to an arbitrary distribution of bulk susceptibility. *Concepts Magn Reson*. 2003;19B(1):26-34. doi:10.1002/cmr.b.10083
3. Jenkinson M, Wilson JL, Jezzard P. Perturbation method for magnetic field calculations of nonconductive objects. *Magn Reson Med*. 2004;52:471-477. doi:10.1002/mrm.20194
4. Marques JP, Bowtell R. Application of a Fourier-based method for rapid calculation of field inhomogeneity due to spatial variation of magnetic susceptibility. *Concepts Magn Reson Part B Magn Reson Eng*. 2005;25B:65-78. doi:10.1002/cmr.b.20034
5. Deistung A, Schweser F, Reichenbach JR. Overview of quantitative susceptibility mapping. *NMR Biomed*. 2017;30:e3569. doi:10.1002/nbm.3569
6. Li L, Leigh JS. Quantifying arbitrary magnetic susceptibility distributions with MR. *Magn Reson Med*. 2004;51:1077-1082. doi:10.1002/MRM.20054
7. Wharton S, Schäfer A, Bowtell R. Susceptibility mapping in the human brain using threshold-based k-space division. *Magn Reson Med*. 2010;63:1292-1304. doi:10.1002/MRM.22334
8. Liu T, Spincemaille P, De Rochefort L, Kressler B, Wang Y. Calculation of susceptibility through multiple orientation sampling (COSMOS): a method for conditioning the inverse problem from measured magnetic field map to susceptibility source image

15222594, 2023, 1, Downloaded from https://onlinelibrary.wiley.com/doi/10.1002/mrm.29627 by Cochrane Portugal, Wiley Online Library on [19/05/2023]. See the Terms and Conditions (https://onlinelibrary.wiley.com/terms-and-conditions) on Wiley Online Library for rules of use; OA articles are governed by the applicable Creative Commons License

in MRI. *Magn Reson Med*. 2009;61:196-204. doi:10.1002/mrm.21828
9. Eskreis-Winkler S, Zhang Y, Zhang J, et al. The clinical utility of QSM: disease diagnosis, medical management, and surgical planning. *NMR Biomed*. 2017;30:e3668. doi:10.1002/nbm.3668
10. Eskreis-Winkler S, Deh K, Gupta A, et al. Multiple sclerosis lesion geometry in quantitative susceptibility mapping (QSM) and phase imaging. *J Magn Reson Imaging*. 2015;42:224-229. doi:10.1002/jmri.24745
11. Wang Y, Spincemaille P, Liu Z, et al. Clinical quantitative susceptibility mapping (QSM): biometal imaging and its emerging roles in patient care. *J Magn Reson Imaging*. 2017;46:951-971. doi:10.1002/jmri.25693
12. Ruh A, Kiselev VG. Calculation of Larmor precession frequency in magnetically heterogeneous media. *Concepts Magn Reson Part A*. 2018;47A:e21472. doi:10.1002/cmr.a.21472
13. Kiselev VG. Larmor frequency in heterogeneous media. *J Magn Reson*. 2019;299:168-175. doi:10.1016/j.jmr.2018.12.008
14. Sandgaard AD, Kiselev VG, Shemesh N, Jespersen SN. Larmor Frequency Shift from Magnetized Cylinders with Arbitrary Orientation Distribution. *NMR Biomed*. 2022;36(3):e4859. doi:10.1002/nbm.4859
15. Yablonskiy DA, Sukstanskii AL. Generalized Lorentzian tensor approach (GLTA) as a biophysical background for quantitative susceptibility mapping. *Magn Reson Med*. 2015;73:757-764. doi:10.1002/mrm.25538
16. Wang Y, Liu T. Quantitative susceptibility mapping (QSM): decoding MRI data for a tissue magnetic biomarker. *Magn Reson Med*. 2015;73:82-101. doi:10.1002/mrm.25358
17. Schweser F, Robinson SD, de Rochefort L, Li W, Bredies K. An illustrated comparison of processing methods for phase MRI and QSM: removal of background field contributions from sources outside the region of interest. *NMR Biomed*. 2017;30(4):e3604. doi:10.1002/NBM.3604
18. Liu J, Liu T, De Rochefort L, et al. Morphology enabled dipole inversion for quantitative susceptibility mapping using structural consistency between the magnitude image and the susceptibility map. *Neuroimage*. 2012;59:2560-2568. doi:10.1016/J.NEUROIMAGE.2011.08.082
19. Milovic C, Bilgic B, Zhao B, Acosta-Cabronero J, Tejos C. Fast nonlinear susceptibility inversion with variational regularization. *Magn Reson Med*. 2018;80:814-821. doi:10.1002/MRM.27073
20. Bilgic B, Pfefferbaum A, Rohlfing T, Sullivan EV, Adalsteinsson E. MRI estimates of brain iron concentration in normal aging using quantitative susceptibility mapping. *Neuroimage*. 2012;59:2625-2635. doi:10.1016/J.NEUROIMAGE.2011.08.077
21. Bilgic B, Fan AP, Polimeni JR, et al. Fast quantitative susceptibility mapping with L1-regularization and automatic parameter selection. *Magn Reson Med*. 2014;72:1444-1459. doi:10.1002/MRM.25029
22. Liu C. Susceptibility tensor imaging. *Magn Reson Med*. 2010;63:1471-1477. doi:10.1002/mrm.22482
23. Ruh A, Scherer H, Kiselev VG. The larmor frequency shift in magnetically heterogeneous media depends on their mesoscopic structure. *Magn Reson Med*. 2018;79:1101-1110. doi:10.1002/mrm.26753
24. Liu T, Liu J, De Rochefort L, et al. Morphology enabled dipole inversion (MEDI) from a single-angle acquisition: comparison with COSMOS in human brain imaging. *Magn Reson Med*. 2011;66:777-783. doi:10.1002/MRM.22816
25. De Rochefort L, Liu T, Kressler B, et al. Quantitative susceptibility map reconstruction from MR phase data using bayesian regularization: validation and application to brain imaging. *Magn Reson Med*. 2010;63:194-206. doi:10.1002/MRM.22187
26. Bilgic B, Xie L, Dibb R, et al. Rapid multi-orientation quantitative susceptibility mapping. *Neuroimage*. 2016;125:1131-1141. doi:10.1016/J.NEUROIMAGE.2015.08.015
27. Karsa A, Shmueli K. SEGUE: a speedy rEgion-growing algorithm for unwrapping estimated phase. *IEEE Trans Med Imaging*. 2019;38:1347-1357. doi:10.1109/TMI.2018.2884093
28. Liu T, Khalidov I, de Rochefort L, et al. A novel background field removal method for MRI using projection onto dipole fields (PDF). *NMR Biomed*. 2011;24(9):1129-1136. doi:10.1002/NBM.1670
29. Liu T, Wisnieff C, Lou M, Chen W, Spincemaille P, Wang Y. Nonlinear formulation of the magnetic field to source relationship for robust quantitative susceptibility mapping. *Magn Reson Med*. 2013;69:467-476. doi:10.1002/MRM.24272
30. Liu Z, Spincemaille P, Yao Y, Zhang Y, Wang Y. MEDI+0: morphology enabled dipole inversion with automatic uniform cerebrospinal fluid zero reference for quantitative susceptibility mapping. *Magn Reson Med*. 2018;79:2795-2803. doi:10.1002/MRM.26946
31. Marques JP, Meineke J, Milovic C, et al. QSM reconstruction challenge 2.0: a realistic in silico head phantom for MRI data simulation and evaluation of susceptibility mapping procedures. *Magn Reson Med*. 2021;86:526-542. doi:10.1002/MRM.28716
32. Bilgic B, Langkammer C, Marques JP, Meineke J, Milovic C, Schweser F. QSM reconstruction challenge 2.0: design and report of results. *Magn Reson Med*. 2021;86:1241-1255. doi:10.1002/MRM.28754
33. Zhou D, Liu T, Spincemaille P, Wang Y. Background field removal by solving the Laplacian boundary value problem. *NMR Biomed*. 2014;27:312-319. doi:10.1002/NBM.3064
34. Milovic C, Tejos C, Acosta-Cabronero J, et al. The 2016 QSM challenge: lessons learned and considerations for a future challenge design. *Magn Reson Med*. 2020;84:1624-1637. doi:10.1002/MRM.28185
35. Fong DCL, Saunders M. LSMR: an iterative algorithm for sparse least-squares problems. *SIAM Journal on Scientific Computing*. Vol 33. Society for Industrial and Applied Mathematics; 2011:2950-2971. doi:10.1137/10079687X
36. Hestenes MR, Stiefel E. Methods of conjugate gradients for solving linear systems 1. *J Res Natl Bur Stand*. 1934;49:409.

SUPPORTING INFORMATION

Additional supporting information may be found in the online version of the article at the publisher's website.

Figure S1. Optimal regularization parameters: (**A**): The optimal weighting parameters for each fitting algorithm, with and without masks (rows) are shown for each of the three algorithms (columns), and for every SNR with finite noise (color-coded). Optimal parameters were found by sweeping through a range of potential values (solid lines), and the parameters that minimized the RMSE was chosen

15222594, 2023, 1, Downloaded from https://onlinelibrary.wiley.com/doi/10.1002/mrm.29627 by Cochrane Portugal, Wiley Online Library on [19/05/2023]. See the Terms and Conditions (https://onlinelibrary.wiley.com/terms-and-conditions) on Wiley Online Library for rules of use; OA articles are governed by the applicable Creative Commons License

for analysis. λ increases since it controls the relative weight of the least squares term, while the others decreases since they control the *l1* or *l2* penalization term. (**B**): The optimal regularization values for each algorithm.

Figure S2. Optimal regularization parameters: The optimal weighting parameters for each fitting algorithm, with and without masks, and with and without background field (BF) are shown for each of the three algorithms. Optimal parameters were found by sweeping through a range of potential values and the parameters that minimized the RMSE was chosen for analysis.

Figure S3. QSM fitting using MEDI w. and w.o. mask: We compare the estimated susceptibility using MEDI for different regularization parameters λ, w. masks and w.o. masks, that (**A**) minimized the RMSE between the two (vertical). For this we considered $\lambda = 1e5$ and $\lambda = 63 \cdot 1e3$, respectively. Next we considered (**B**) the estimated susceptibility that produced the same least squares $LS_\Omega = \left\|(\vec{\Omega} - \mathbf{A}\vec{\chi})\right\|_2$. For this we chose $\lambda = 1e5$ and $\lambda = 35 \cdot 1e3$, respectively. Lastly, we considered (**C**) the susceptibility with the same norm $\|\vec{\chi}\|_2$ by chosing $\lambda = 26 \times 10^3$ and $\lambda = 63 \times 10^3$, respectively. All three cases show substantial changes in susceptibility estimation, and contrast, which is visible from looking at the relative error.

Figure S4. QSM fitting using COSMOS w. and w.o. masks: Here we compare susceptibility fits using data from the QSM reconstruction challenge 1.0. This includes signals acquired at 12 different sample orientations. While the contrast appears very similar, the difference map reveals noticeable differences resulting in 24% RMSE between the two fits w. and w.o. masks in fitting algorithm.

How to cite this article: Sandgaard AD, Shemesh N, Jespersen SN, Kiselev VG. To mask or not to mask? Investigating the impact of accounting for spatial frequency distributions and susceptibility sources on QSM quality. *Magn Reson Med*. 2023;90:353-362. doi: 10.1002/mrm.29627

15222594, 2023, 1, Downloaded from https://onlinelibrary.wiley.com/doi/10.1002/mrm.29627 by Cochrane Portugal, Wiley Online Library on [19/05/2023]. See the Terms and Conditions (https://onlinelibrary.wiley.com/terms-and-conditions) on Wiley Online Library for rules of use; OA articles are governed by the applicable Creative Commons License